Observation of the Fluctuation Spin Hall Effect in a Low-Resistivity Antiferromagnet

Chi Fang, Caihua Wan,* Xiaoyue Zhang, Satoshi Okamoto, Tianyi Ma, Jianying Qin, Xiao Wang, Chenyang Guo, Jing Dong, Guoqiang Yu, Zhenchao Wen, Ning Tang, Stuart S. P. Parkin, Naoto Nagaosa, Yuan Lu,* and Xiufeng Han*

Cite This: https://doi.org/10.1021/acs.nanolett.3c03085 | Read Online

ACCESS | 📊 Metrics & More | 📑 Article Recommendations | 🆂🅸 Supporting Information

ABSTRACT: The spin Hall effect (SHE) can generate a pure spin current by an electric current, which is promisingly used to electrically control magnetization. To reduce the power consumption of this control, a giant spin Hall angle (SHA) in the SHE is desired in low-resistivity systems for practical applications. Here, critical spin fluctuation near the antiferromagnetic (AFM) phase transition in chromium (Cr) is proven to be an effective mechanism for creating an additional part of the SHE, named the fluctuation spin Hall effect. The SHA is significantly enhanced when the temperature approaches the Néel temperature (T_N) of Cr and has a peak value of -0.36 near T_N. This value is higher than the room-temperature value by 153% and leads to a low normalized power consumption among known spin−orbit torque materials. This study demonstrates the critical spin fluctuation as a prospective way to increase the SHA and enriches the AFM material candidates for spin−orbitronic devices.

KEYWORDS: spin Hall effect, spin fluctuation, antiferromagnet, chromium, low-power devices

The spin Hall effect (SHE) utilizes spin−orbit coupling to convert a longitudinal charge current j_c into a transverse pure spin current j_s. Because of the ability to electrically control magnetization by spin−orbit torque, the SHE shows promising applications in magnetic random-access memory (MRAM),[1−3] programmable logic devices,[4,5] and microwave nano-oscillators.[6] Spin Hall angles (SHA, θ_{SH}), defined as the ratio between spin Hall conductivity σ_{SH} and longitudinal conductivity σ, are parameters that characterize the efficiency of transforming the j_c into the j_s or vice versa. Accompanied by a high σ, θ_{SH} is the key factor for reducing writing power and achieving the high efficiency of spin−orbit torque (SOT) devices.[7] Thus, the development of materials and/or the exploration of physics to improve θ_{SH} in low-resistivity systems is appealing.[8,9]

The microscopic mechanisms behind the SHE can be categorized into three classes: the intrinsic one due to the nontrivial Berry curvatures of electronic band structures and the other two extrinsic ones, the side-jump (sj) and skew-scattering (ss) mechanisms.[8] Inspired by the mechanisms, several effective means have been explored to enhance the SHA, such as adopting heavy elements,[10−15] electronic structure engineering,[16−18] doping,[7,19,20] interface decoration,[21] and superlattice stacking.[22]

Distinguished from the SHE in normal metals, here, the fluctuation spin Hall effect (FSHE) is relevant to only the extrinsic mechanisms because only fluctuation of a spin lattice activated thermally is involved, which can evidence the significance of the extrinsic mechanisms to the overall SHE.
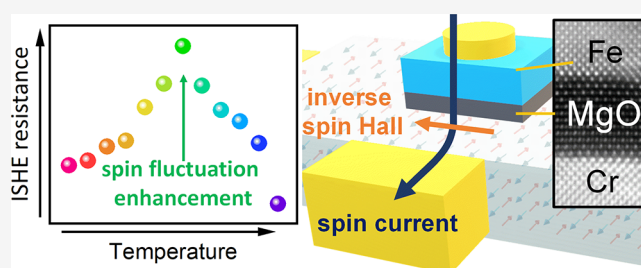
The FSHE is attributed to the combinations of several individual scattering processes between conduction electrons and local spins as explained in below, instead of a single process accounting for the SHE. These involved local spins are needed to maintain the correlation within a certain correlation length ξ as shown in Figure 1a, which thus makes the FSHE process sensitive to temperature, especially at the critical point of the phase change.

Recently, critical spin fluctuation in magnetically ordered systems at their magnetic phase transition temperatures was reported to nontrivially result in an increased θ_{SH} by intensifying interaction of delocalized electrons with local spins in ferromagnets (FMs).[23−25] For antiferromagnets, Saglam et al.[26] evidenced that spin fluctuation of the antiferromagnetic FeMn at its Néel temperature (T_N) increased the θ_{SH} of the $Ni_{80}Fe_{20}$/FeMn/W trilayer in a spin-pumping experiment. Frangou et al.[27] and Wang et al.[28] addressed the key role of spin fluctuation in the enhancement of the transmission parameter of the FM/IrMn interface near T_N. Although there
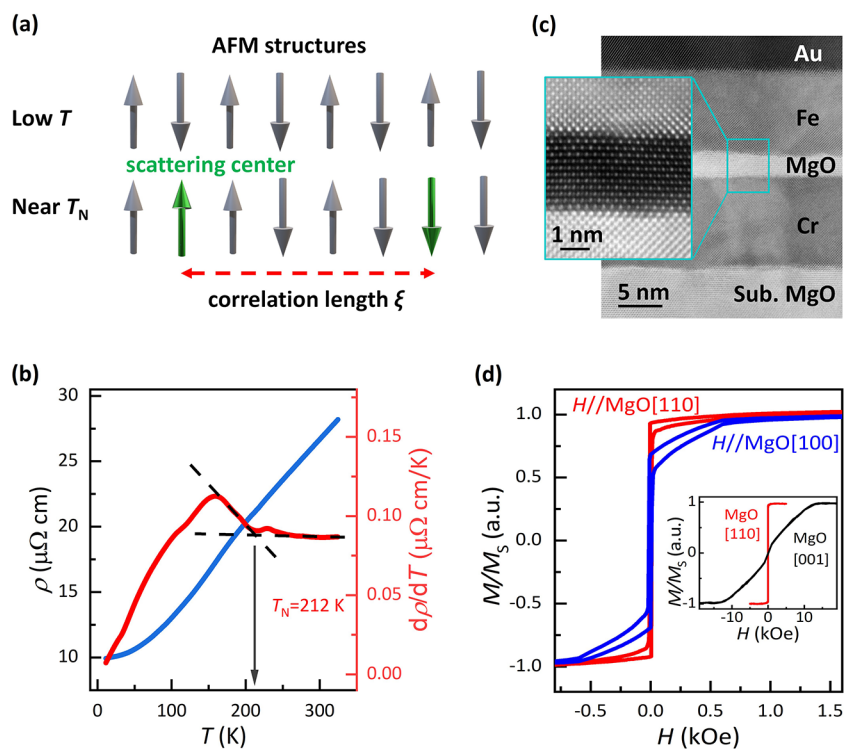
Figure 1. Spin fluctuation in single-crystal Cr stacks. (a) Correlation length ξ of antiferromagnetic materials. The gray arrows are the magnetic spins forming the AFM order. Green arrows act as the scattering centers activated by spin fluctuation. ξ represents the correlation length within which the scattering centers can correlate with each other in an antiparallel manner. ξ becomes divergent with T approaching T_N. (b) Temperature dependence of resistivity (blue line) and its differential with respect to T (red line) in 10 nm Cr. T_N is determined to be 212 K. Black dashed lines are a guide for the eyes. (c) High-resolution cross-sectional transmission electron microscope (HRXTEM) pattern of the junction. Flat interfaces are indicated. The inset shows a black field image of the region near the MgO barrier. Epitaxy relation was well defined globally throughout the sample. Cr and Fe lattices grew along the MgO [001] direction. (d) Magnetic hysteresis loop of Cr/MgO/Fe/Au films with an external magnetic field along $[110]_{MgO}$ (red, also noted as in plane) and $[100]_{MgO}$ (blue). The inset shows $[001]_{MgO}$ (black, also noted as out of plane) and reproduction of $[110]_{MgO}$ to show the in-plane easy axis of the Fe layer.

is no direct experimental evidence of the contribution of antiferromagnetic (AFM) spin fluctuation to the bulk SHE, these magnetic systems have clearly hinted at the significant role of spin fluctuations in the phenomenally enhanced SHE; however, all of the systems mentioned above contain interfaces with ferromagnetic films, which lack the simplicity to highlight the bulk SHE from possibly entangled interfacial effects such as spin mixing conductance, spin memory loss, and magnetic proximity effects. An elaborately designed AFM system without any FM/AFM interfaces can promisingly provide a clearer platform for investigating the influence of spin fluctuations on the bulk SHE.

Among antiferromagnets, polycrystalline Cr has already shown a sizable θ_{SH} from −0.051 to −0.09 and low resistivity as a candidate SOT source.[29−31] However, the relevance of its spin Hall effect with its antiferromagnetic order has not been uncovered, which is also rare with respect to other antiferromagnets from a broader perspective. Here, we furthermore choose epitaxial Cr single-crystalline films sandwiched by MgO as the AFM material to uncover the FSHE originating from the influence of spin fluctuations on the SHE near its T_N. A large θ_{SH} of −0.36 at 225 K is demonstrated by measuring the inverse spin Hall effect (ISHE) and direct spin Hall effect (DSHE) with the spin Hall tunneling spectrum (SHTS) method for the Cr/MgO/Fe magnetic tunnel junctions (MTJs). σ_{SH}/σ^2, as an indicator of the spin fluctuation contribution, followed a clear power law with T, consistent with the modeled one in FSHE.

Chromium is an itinerant antiferromagnet with collinear spin sublattices and a simple body-centered cubic (bcc) structure. The T_N of bulk Cr is 311 K and can be decreased by reducing the thickness. A single 10 nm Cr layer was prepared on MgO (001) and fabricated into a four-probe bar to determine the T_N of Cr. As shown in Figure 1b, resistivity ρ increased further due to the disorder-induced scattering via spin fluctuation near T_N.[32,33] Differential resistivity ρ with respect to T, i.e., $d\rho/dT$, captured this enhancement clearly. Above 212 K, $d\rho/dT$ maintained a stable platform with a small slope. From 212 K to lower temperatures, $d\rho/dT$ began to acquire an extra slope, because spin fluctuation scattering was switched on in this case. With a further decrease in T and freezing of the AFM structure, after a peak at 150 K, $d\rho/dT$ finally approached a smaller but stable value due to the decrease in magnon density. This behavior, similar to that described in ref 33, indicated the T_N of Cr was ∼212 K. This value is near the T_N of 235 K of the epitaxial 50 nm Cr layer.[33]

To investigate the SHE in Cr, the SHTS setup[34,35] was adopted. High-quality epitaxial Cr(t)/MgO(2.3 nm)/Fe(10 nm)/Au(5 nm) stacks (t = 7, 10, 25, and 50 nm) were deposited on MgO (001) substrates by molecular-beam epitaxial growth as shown in Figure 1c (also see section I of the Supporting Information). The Fe layer was used as a spin polarizer of charge current, and the Cr layer functioned as a spin analyzer to convert a spin current into a transverse voltage via the ISHE. Figure 1d and its inset show the magnetic hysteresis loops as magnetic field H applied along the in-plane $[110]_{MgO}$ and $[100]_{MgO}$ and out-of-
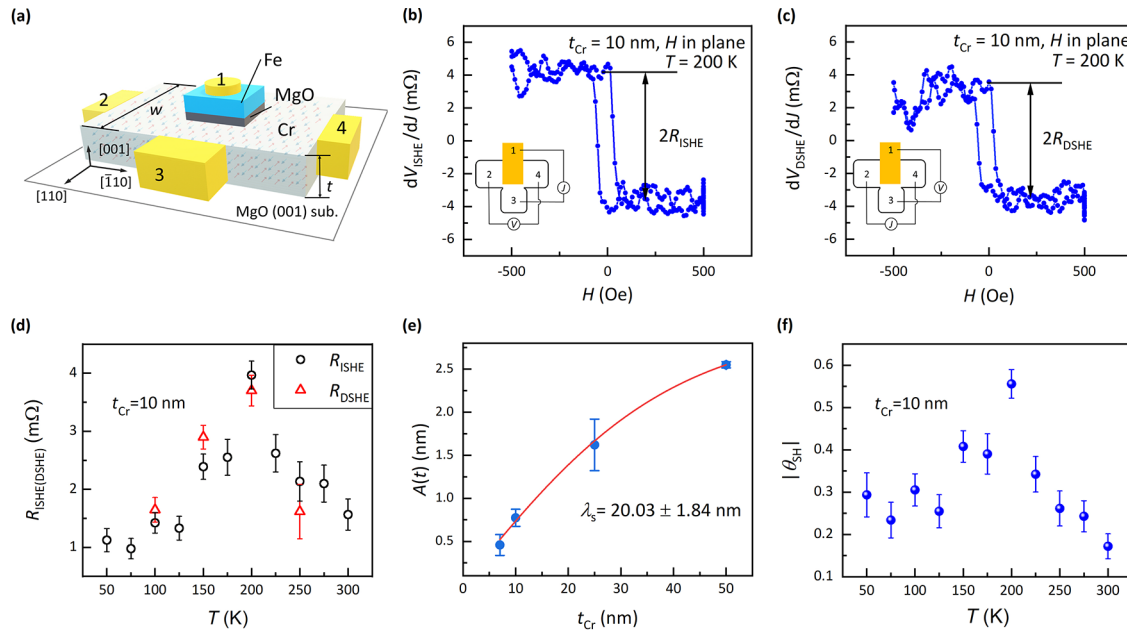
Figure 2. Detection of the FSHE with the ISHE and DSHE setup. (a) Schematic diagram of fabricated MTJ devices. (b) ISHE and (c) DSHE in 10 nm Cr with an in-plane magnetic field along MgO [110] at 200 K. The inset shows a schematic diagram of measurement of the ISHE with current J loaded between electrodes 1 and 3 and V_{ISHE} collected between electrodes 2 and 4 and the DSHE upon exchange of the source and measurement meters. $R_{ISHE(DSHE)}$ represents the saturated value of $dV_{ISHE(DSHE)}/dJ$. (d) Critical spin fluctuation enhanced R_{ISHE} (black circles) and R_{DSHE} (red triangles) resistance in the MTJ device. The magnitude of $2R_{ISHE(DSHE)}$ is given by the difference between intercepts of linear fitting of two resistance platforms, and the error bar is the standard error of the linear fitting. (e) Thickness dependence of factor $A(t)$. The red line is the fitting result following eq 2. (f) Temperature dependence of the SHA.

plane $[001]_{MgO}$ directions by a vibrating sample magnetometer (VSM). The loops verified the in-plane easy axis along the $[110]_{MgO}$ direction. This epitaxial relation contributed to the formation of the magnetic easy axis of Fe and the AFM ordering of Cr along the $[110]_{MgO}$ direction owing to the magneto-crystalline anisotropy.

The raw stacks were fabricated into 6 μm × 6 μm MTJs with one top electrode and three bottom electrodes (Figure 2a) with standard ultraviolet lithography and an ion-beam etching process. The junction is surrounded by oxide SiO_2 or Al_2O_3 to isolate the top electrode and bottom electrodes. Before measurement, magnetic field cooling is applied along $[110]_{MgO}$ to align magnetization and enhance anisotropy in Fe, i.e., $\mathbf{M}_{Fe}$. To detect the ISHE as shown in Figure 2b, an ac current J was injected between electrodes 1 and 3 (Figure 2b, inset) with an amplitude of 20−50 μA and a frequency of 8.3 Hz by a Keithley 6221 instrument and the voltage was detected with a lock-in amplifier (SR830) for samples under certain magnetic field and temperature conditions. Only the first harmonic signals are picked up to disentangle with any thermoelectric artifacts. A preamplifier (SR560) was used to improve the signal-to-noise ratio. As the $\mathbf{M}_{Fe}$ stayed along $[110]_{MgO}$, the injected current was spin-polarized along $[110]_{MgO}$ before electrons tunneled through the MgO barrier and entered the Cr. The SHE in Cr led to the transverse scattering of the tunneling spin current along the $[\bar{1}10]_{MgO}$ direction so that an electric field between electrodes 2 and 4 was built as $V_{ISHE} \propto \theta_{SH}(\mathbf{j}_s \times \mathbf{s})$. The $\mathbf{j}_s$ indicates the flowing direction of the spin current along the film normal and the $\mathbf{s}$ indicates the spin-polarized direction determined by $\mathbf{M}_{Fe}$. When H was in plane and parallel or antiparallel to $[110]_{MgO}$, $(\mathbf{j}_s \times \mathbf{s})$ reached its positive or negative maximum and so did the dV_{ISHE}/dJ whose maximum absolute value was R_{ISHE}. When the H direction was fixed, the R_{ISHE} measured in Cr had

the same (opposite) sign as in Ta (Pt), indicating Cr has a negative θ_{SH}. This observation was in accord with the previous reports.[29,30,34,35]

To observe the FSHE, we performed the SHTS measurement on a t_{Cr} = 10 nm sample at different temperatures from 50 to 300 K with an interval of 25 K. The extracted R_{ISHE} values are plotted in Figure 2d. Below the critical point, 212 K, R_{ISHE} increased rapidly with T. Above 212 K, R_{ISHE} decreased with a further increase in T. The T_{max} at which R_{ISHE} was maximized was quite near T_N. This enhancement behavior in the temperature dependence is also observed in other samples (as shown in section II of the Supporting Information). To eliminate any possible contributions from the spin transport artifacts in Fe, we also adopted the DSHE[35] setup for the same device (Figure 2c). In the DSHE measurement, a current was applied between electrodes 2 and 4, which produced a spin accumulation at the Cr/MgO interface. A DSHE voltage V_{DSHE} was then detected by the Fe electrode because of the spin accumulation at the Cr/MgO interface. The magnitude of V_{DSHE} is then proportional to $\mathbf{M}_{Fe}$.[36,37] V_{DSHE} and thus $R_{DSHE} = (dV_{DSHE}/dJ)_{max}$ across the MTJ were recorded between electrodes 1 and 3 to evaluate the SHE (Figure 2c, inset). In this setup, no current flowed through the Fe layer, so V_{DSHE} had no chance to be involved with any magnetotransport artifacts in Fe. The T dependence of R_{DSHE} also showed an enhancement at 200 K, coinciding with the ISHE result. Both T dependencies indicated an enhancement of the SHE near the T_N of Cr, which was attributed to the enhanced fluctuation of local spins near T_N as quantitively analyzed below. In addition, R_{ISHE} and R_{DSHE} are ∼3.97 and ∼3.70 mΩ in panels b and c, respectively, of Figure 2, close to each other and as expected from the Onsager relation; their small discrepancy may result from different measurement geometries.
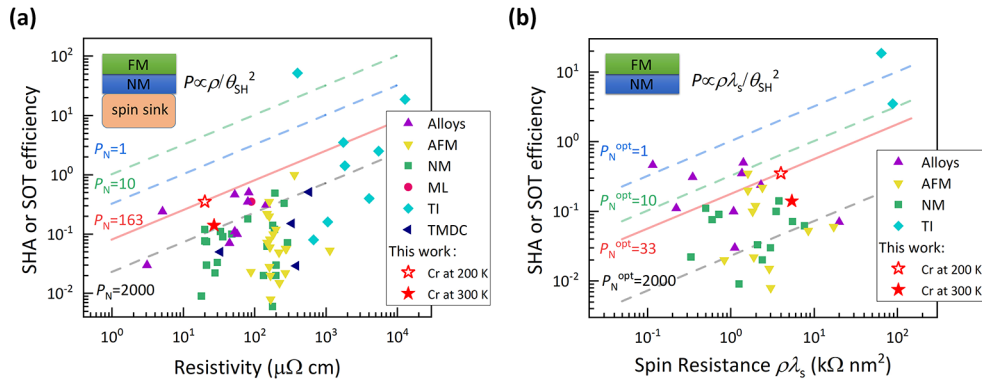
Figure 3. Summary of the normalized power consumption in SOT materials. (a) $P_N = \rho/\theta_{SH}^2$ with a spin sink. (b) $P_N^{opt} = \rho\lambda_s/\theta_{SH}^2$ without a spin sink. Resistivity ρ and magnitude of SHA or SOT efficiency θ_{SH} are two key parameters of P_N. Spin diffusion length λ_s is further considered for an optimal power P_N^{opt} of its thickness dependence. Dash or solid lines represent the contour lines of P_N (or P_N^{opt}) values of 1 (blue dashed line), 10 (green dashed line), 163 (or 33) (same level as this work, red solid line), and 2000 (gray dashed line) $\mu\Omega$ cm (or kΩ nm^2). The data points are from Cr in this work (empty red star at 200 K and filled red star at 300 K) and published works on NMs (nonmagnetic metals, green squares), MLs (insert or multilayers, pink circle), alloys (purple triangles), AFMs (antiferromagnets, yellow triangles), TIs (topological insulators, light blue diamonds), and TMDCs (transition metal dichalcogenide, dark blue triangles). The values of ρ, θ_{SH}, and λ_s are listed in a table in section III of the Supporting Information.
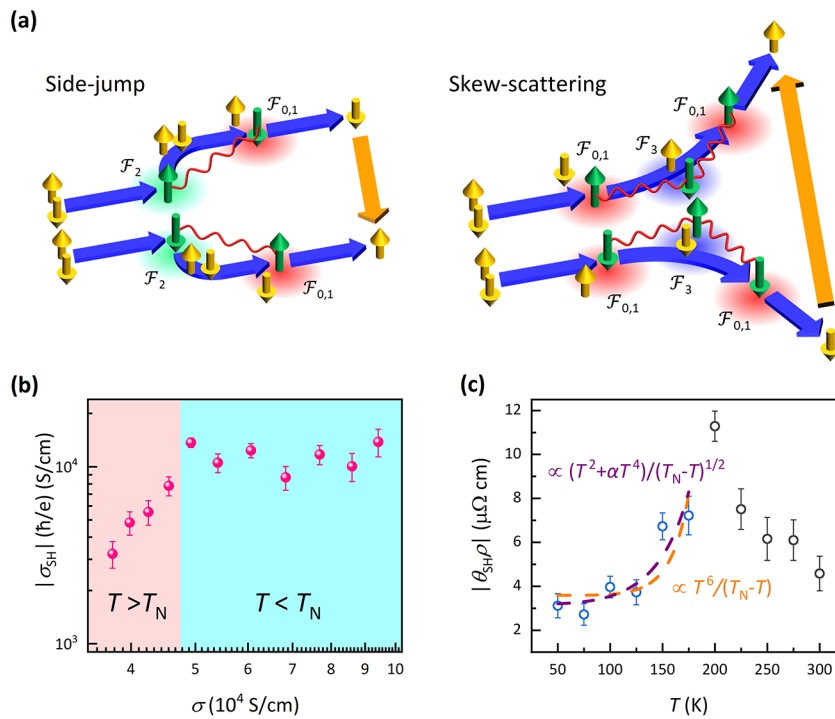

Figure 4. Fluctuation spin Hall effect in Cr. (a) Antiferromagnetic spin fluctuation. Spin current (orange arrows) is caused by AFM spin fluctuation. Yellow arrows are conduction electron spins, and green arrows are local spins. In the $\mathcal{F}_{2(3)}$ scattering processes, the deflected direction of scattered electrons depends on the direction of the local spins (the conductive electron spins), combining $\mathcal{F}_{0,1}$ to form the side-jump-type (skew-scattering-type) contribution to σ_{SH}. The red wavy curves represent the propagators of AFM spin fluctuation, which relates to the correlation length. (b) Scaling relation between conductivity and spin Hall conductivity. The scaling law is different below (blue shadow) and above (pink shadow) the T_N. (c) Temperature dependence of the product of SHA and resistivity. The purple dashed line shows the fitting result of the relation $\sigma_{SH}^{sj}/\sigma^2 \propto (T^2 + \alpha T^4)/\sqrt{T_N - T}$ with an adjusted R^2 (coefficient of determination) of 0.74. The orange dashed line shows the fitting result of the relation $\sigma_{SH}^{ss}/\sigma^2 \propto T^6/(T_N - T)$ with an adjusted R^2 of 0.51. For these fittings, we consider the temperature range of 50−175 K.

For the same spin polarizer and setup, dV_{ISHE}/dJ depends on the intrinsic properties of the spin analyzer material, which enables the SHTS to characterize spin Hall materials.[34,35] To qualify the enhancement, we calculated θ_{SH} at different temperatures. θ_{SH} can be deduced from eq 1 given by Liu et al.[35]

$$R_{ISHE} = \left(\frac{dV_{ISHE}}{dJ}\right)_{max} = \frac{\theta_{SH}P\rho}{w} \times \frac{\lambda_s}{t} \times \tanh(t/2\lambda_s) \tag{1}$$

where P denotes the spin polarization of the FM layer, λ_s is the spin diffusion length of Cr, and t and w are the thickness and channel width of the Cr layer, respectively. Thus, given the R_{ISHE} values and other mentioned parameters, one can estimate the

θ_{SH} of the Cr layer. To estimate θ_{SH}, λ_s in Cr[29,30,38] is required and could be derived by fitting

$$wtR_{ISHE}/(P\rho) = \theta_{SH}\lambda_s \tanh(t/2\lambda_s) = A(t) \qquad (2)$$

We used the parameters at 300 K to determine a λ_s of 20.03 ± 1.84 nm (Figure 2e). With this temperature-insensitive λ_s, θ_{SH} could be calculated from eq 1. With calibrated P by saturation magnetization M_S for the single-crystal Fe/MgO electrode[39] (section I of the Supporting Information), $w = 10 \mu m$, $t = 10$ nm, and $\rho = 21.93 \mu\Omega$ cm (sections I and II of the Supporting Information), Sample 1 shown in Figure 2b−d gives the highest values of $|\theta_{SH}|$ of 0.56 ± 0.03 at 200 K and 0.17 ± 0.03 at 300 K (Figure 2f), whose uncertainty is given by the linear fitting of the two resistance platforms of R_{ISHE} (section II of the Supporting Information). To check the reproducibility of the FSHE enhancement in Cr and also take the sample and process variations into account, we measured two other samples (section II of the Supporting Information). The peak value of the average R_{ISHE} of the three samples was 2.74 ± 0.59 mΩ at 225 K, so we have an average $|\theta_{SH}|$ of 0.36 ± 0.08 at 225 K. Likely, the average $|\theta_{SH}| = 0.14 ± 0.02$ at 300 K. The 300 K value is comparable to but higher than the literature values[31] of −0.051 to −0.09, probably due to the lack of a magnetic interface here. Moreover, spin fluctuation near T_N caused a remarkable enhancement in the SHA of 153% at 225 K compared to that at 300 K. The 225 K value has already been comparable to that of heavy metals,[40] inferring Cr can function as an efficient SOT source.

In addition, the Cr film has a relatively low resistivity of ~27 $\mu\Omega$ cm at room temperature, nearly 1 order of magnitude lower than the values of ~190 $\mu\Omega$ cm of the β-phase Ta[10] and 100−300 $\mu\Omega$ cm of the β-phase W[15] systems, which can further improve its energy efficiency. We adopted the normalized power consumption[41] $P_N = \rho/\theta_{SH}^2$ to evaluate Cr as a SOT material. As shown in Figure 3a, Cr has a relatively low power consumption compared to the reported values. Notably, this estimation ignores the backflow of spin current in the $t \leq \lambda_s$ case because the spin backflow issue can be mitigated by a neighboring spin sink in applications. An estimation of optimal power consumption $P_N^{opt} = \rho\lambda_s/\theta_{SH}^2$ considering the reduced effective SHA by the spin backflow issue in a single-SOT material is also shown in Figure 3b. Section III of the Supporting Information shows a comparison of these two methods based on theoretical calculation of the spin diffusion model. These merits, the large SHA and low resistivity, persist below or around T_N, which facilitates the use of Cr as a SOT channel material in spin−orbitronics devices.

In theory, when the spin fluctuation near the Curie temperature (T_C) was taken into account, Kondo first developed a theory to explain the anomalous Hall effect in ferromagnets.[42] It is further generalized to account for the SHE and ISHE by considering the short-range spin−spin interaction[43] and the long-range dynamical correlation among localized moments.[44] Okamoto et al.[44] derived spin Hall conductivity σ_{SH}^{sj} and σ_{SH}^{ss}, which predict the nontrivial SHA enhancement around the ferromagnetic quantum critical point due to the critical spin fluctuations. For the AFM spin fluctuation, while the individual scattering processes $\mathcal{F}_{0,1}$, $\mathcal{F}_2$, and $\mathcal{F}_3$ (defined in ref 44 and schematically shown in Figure 4a) remain the same as those in the ferromagnetic case, the microscopic mechanisms of the side-jump and skew-scattering contributions (Figure 4a) to the FSHE require further development[45] (section IV of the Supporting Information). Schematically, the microscopic details

of the two mechanisms consist of three scattering processes. The $\mathcal{F}_{0,1}$ process contributes 180 ° back-scattering of antiparallelly polarized conduction electrons (yellow arrow) with local spins (green arrow). The $\mathcal{F}_2$ and $\mathcal{F}_3$ processes result in transverse scattering of electrons depending on the polarization of local spins and scattered electron spins, respectively.[44] Thus, the sequential scattering due to the $\mathcal{F}_{0,1}$ and $\mathcal{F}_2$ ($\mathcal{F}_3$) processes gives rise to the transverse spin current, leading to the side-jump (skew-scattering) mechanism in the FSHE. Temperature is involved in FSHE processes in two ways: (1) more dynamical spins, functioning as the local scattering centers, are activated with the increase in T toward the ordering temperature as shown in Figure 1a, and (2) correlation length ξ between the dynamically activated local spins increases as T approaches the ordering temperature from above and below, each of which favors the sequential occurrence of the $\mathcal{F}_{0,1}$ and $\mathcal{F}_2$ ($\mathcal{F}_3$) processes in a higher probability. Specifically, one would then expect a clear enhancement of the SHE in an antiferromagnetic system around its Néel temperature, at which the correlation length diverges. This hypothesis is instructive for experimentally studying the influence of AFM spin fluctuations on the bulk FSHE in the clean Cr/MgO/Fe MTJs and for developing corresponding theories on mechanisms of the SHE.[46]

To examine the mechanism of the observed SHE, the scaling relation between spin conductivity σ_{SH} and conductivity σ of Cr is plotted in Figure 4b. The scaling relation does not simply follow the $\sigma_{SH} \propto$ constant relation for the side-jump or intrinsic mechanism or the $\sigma_{SH} \propto \sigma$ relation for the skew-scattering mechanism. A clear change in the scaling property at T_N is seen rather than a gradual crossover behavior.[47]

Equation 1 shows that the main factor contributing to the enhanced R_{ISHE} was $\sigma_{SH}/\sigma^2 = \theta_{SH}\rho$. Normally, both spin polarization P and the term $\frac{\lambda_s}{t} \times \tanh(t/2\lambda_s)$ remain stable or decrease slightly and monotonically as T increases.[48−50] The P contribution is calibrated by M_s (section I of the Supporting Information), and λ_s remains the same as the 300 K value, which could at most introduce a 2% overestimation of θ_{SH} or σ_{SH} (section II of the Supporting Information) as λ_s may increase as T decreases. Consequently, these two terms could not account for the significantly increasing R_{ISHE} below T_N. Figure 4c shows the T dependence of $|\theta_{SH}\rho|$. When the skew scattering provides the dominant contribution to the SHE, $|\theta_{SH}\rho|$ serves as an indicator of the SOC strength suggested in ref 44. $|\theta_{SH}\rho|$ followed a $T^{3.06}$ power law at low $T < T_{max}$ (section V of the Supporting Information). While this power law appears to be similar to the predicted $T^{10/3}$ behavior of FM with a T_C of 0, an AFM material with a non-zero T_N should have power laws different than this prediction (section IV of the Supporting Information) and a different power of the enhancement factor $\delta = |T - T_{N,C}|$ approaching the magnetic transition temperature (discussion in ref 46). Note the $\mathcal{F}_{0,1}$ and $\mathcal{F}_2$ ($\mathcal{F}_3$) processes also take place in AFM materials; their manner of cooperation is different from that of a FM material. The long-range dynamical correlation length among spins as the scattering centers, which determines the probability of the sequential occurrence of the $\mathcal{F}_{0,1}$ and $\mathcal{F}_2$ ($\mathcal{F}_3$) processes, differs between AFM and FM materials. These factors jointly result in a T power law in Cr different from the FM fluctuation. When considering AFM spin fluctuation, the Kondo model could be generalized to give the relation $\sigma_{SH}^{ss}/\sigma^2 \propto T^6/(T_N - T)$ for the skew-scattering mechanism and the relation

$\sigma_{\mathrm{SH}}^{\mathrm{sj}}/\sigma^2 \propto (T^2 + \alpha T^4)/\sqrt{T_{\mathrm{N}} - T}$ for the side-jump mechanism (section IV of the Supporting Information; also see ref 46), where α is a constant deduced from the T dependence of ρ (section V of the Supporting Information). Both models could give a reasonable fit to the experimental data, as shown in Figure 4c; however, the side-jump mechanism gives a higher degree of fitting confidence, which might dominate the FSHE more here.

Above T_{N}, the AFM spin texture of Cr is no longer stable. The electron−phonon and electron−electron interactions that weakly depend on spins gradually dominate the T dependence of the momentum relaxation process with a T^5 law[51,52] and a T^2 law,[53] respectively. These spin-irrelevant processes contribute more to momentum-relaxation scatterings than the spin fluctuation mechanism. As a natural result, $\theta_{\mathrm{SH}}\rho$ was inclined to decrease gradually.

In conclusion, we investigated the bulk spin Hall angles and its temperature dependence of Cr in Cr/MgO/Fe fully epitaxial MTJs without a direct contact between Cr and Fe. Critical spin fluctuation enhancement of θ_{SH} to −0.36 in Cr by 153% near the T_{N} of 212 K compared to 300 K was observed. The dependence of $\theta_{\mathrm{SH}}\rho$ on T before T_{N} was experimentally measured and fitted with the modeled T dependence of the AFM spin fluctuation. This effective mechanism of increasing spin Hall angles can be instructive for the design of antiferromagnets with much larger spin Hall angles and low resistivity and further advance AFM applications in SOT devices.

■ ASSOCIATED CONTENT

Data Availability Statement

The data that support the findings of this study are available from the corresponding author upon reasonable request.

ⓢ Supporting Information

The Supporting Information is available free of charge at https://pubs.acs.org/doi/10.1021/acs.nanolett.3c03085.

> Sample preparation and characterization; original data of the ISHE and DSHE with an in-plane or out-of-plane magnetic field, the ISHE with different Cr thicknesses or measuring currents, extraction of R_{ISHE} or R_{DSHE}, data from other samples, shunting factor and temperature dependence of spin Hall conductivity; normalized power consumption; theoretical consideration of the SHE by AFM spin fluctuation; and fitting details of resistivity and $\theta_{\mathrm{SH}}\rho$ (PDF)

■ AUTHOR INFORMATION

Corresponding Authors

Caihua Wan − *Beijing National Laboratory for Condensed Matter Physics, Institute of Physics, University of Chinese Academy of Sciences, Chinese Academy of Sciences, Beijing 100190, China; Songshan Lake Materials Laboratory, Dongguan, Guangdong 523808, China;* Email: wancaihua@iphy.ac.cn

Yuan Lu − *Université de Lorraine, CNRS, Institut Jean Lamour, UMR 7198, 54011 Nancy, France;* ⓘ orcid.org/0000-0003-3337-8205; Email: yuan.lu@univ-lorraine.fr

Xiufeng Han − *Beijing National Laboratory for Condensed Matter Physics, Institute of Physics, University of Chinese Academy of Sciences, Chinese Academy of Sciences, Beijing 100190, China; Songshan Lake Materials Laboratory, Dongguan, Guangdong 523808, China; Center of Materials Science and Optoelectronics Engineering, University of Chinese Academy of Sciences, Beijing 100049, China;* ⓘ orcid.org/0000-0001-8053-793X; Email: xfhan@iphy.ac.cn

Authors

Chi Fang − *Beijing National Laboratory for Condensed Matter Physics, Institute of Physics, University of Chinese Academy of Sciences, Chinese Academy of Sciences, Beijing 100190, China; Max Planck Institute of Microstructure Physics, Halle (Saale) 06120, Germany;* ⓘ orcid.org/0000-0001-6827-1913

Xiaoyue Zhang − *Université de Lorraine, CNRS, Institut Jean Lamour, UMR 7198, 54011 Nancy, France; State Key Laboratory of Artificial Microstructure and Mesoscopic Physics, School of Physics, Peking University, Beijing 100871, China*

Satoshi Okamoto − *Materials Science and Technology Division, Oak Ridge National Laboratory, Oak Ridge, Tennessee 37831, United States;* ⓘ orcid.org/0000-0002-0493-7568

Tianyi Ma − *Beijing National Laboratory for Condensed Matter Physics, Institute of Physics, University of Chinese Academy of Sciences, Chinese Academy of Sciences, Beijing 100190, China; Université de Lorraine, CNRS, Institut Jean Lamour, UMR 7198, 54011 Nancy, France;* ⓘ orcid.org/0000-0002-5987-6459

Jianying Qin − *Beijing National Laboratory for Condensed Matter Physics, Institute of Physics, University of Chinese Academy of Sciences, Chinese Academy of Sciences, Beijing 100190, China; Université de Lorraine, CNRS, Institut Jean Lamour, UMR 7198, 54011 Nancy, France*

Xiao Wang − *Beijing National Laboratory for Condensed Matter Physics, Institute of Physics, University of Chinese Academy of Sciences, Chinese Academy of Sciences, Beijing 100190, China*

Chenyang Guo − *Beijing National Laboratory for Condensed Matter Physics, Institute of Physics, University of Chinese Academy of Sciences, Chinese Academy of Sciences, Beijing 100190, China*

Jing Dong − *Beijing National Laboratory for Condensed Matter Physics, Institute of Physics, University of Chinese Academy of Sciences, Chinese Academy of Sciences, Beijing 100190, China*

Guoqiang Yu − *Beijing National Laboratory for Condensed Matter Physics, Institute of Physics, University of Chinese Academy of Sciences, Chinese Academy of Sciences, Beijing 100190, China; Songshan Lake Materials Laboratory, Dongguan, Guangdong 523808, China;* ⓘ orcid.org/0000-0002-7439-6920

Zhenchao Wen − *National Institute for Materials Science (NIMS), Tsukuba, Ibaraki 305-0047, Japan*

Ning Tang − *State Key Laboratory of Artificial Microstructure and Mesoscopic Physics, School of Physics, Peking University, Beijing 100871, China;* ⓘ orcid.org/0000-0003-2576-523X

Stuart S. P. Parkin − *Max Planck Institute of Microstructure Physics, Halle (Saale) 06120, Germany;* ⓘ orcid.org/0000-0003-4702-6139

Naoto Nagaosa − *RIKEN Center for Emergent Matter Science (CEMS), Wako 351-0198, Japan*

Complete contact information is available at:
https://pubs.acs.org/10.1021/acs.nanolett.3c03085

Author Contributions

C.F. and C.W. contributed equally to this work. C.F. and C.W. conceived and designed the experiment. S.O. and N.N. performed the theoretical analysis. Y.L., X.Z., T.M., and J.Q. grew the single-crystal films. C.F., X.W., C.G., and J.D. carried

■ REFERENCES

(1) Yu, G.; Upadhyaya, P.; Fan, Y.; Alzate, J. G.; Jiang, W.; Wong, K. L.; Takei, S.; Bender, S. A.; Chang, L.-T.; Jiang, Y.; et al. Switching of perpendicular magnetization by spin-orbit torques in the absence of external magnetic fields. *Nat. Nanotechnol.* **2014**, *9* (7), 548.

(2) Fukami, S.; Zhang, C.; DuttaGupta, S.; Kurenkov, A.; Ohno, H. Magnetization switching by spin-orbit torque in an antiferromagnet-ferromagnet bilayer system. *Nat. Mater.* **2016**, *15* (5), 535.

(3) Oh, Y.-W.; Baek, S.-H. C.; Kim, Y. M.; Lee, H. Y.; Lee, K.-D.; Yang, C.-G.; Park, E.-S.; Lee, K.-S.; Kim, K.-W.; Go, G.; et al. Field-free switching of perpendicular magnetization through spin-orbit torque in antiferromagnet/ferromagnet/oxide structures. *Nat. Nanotechnol.* **2016**, *11* (10), 878.

(4) Wan, C.; Zhang, X.; Yuan, Z.; Fang, C.; Kong, W.; Zhang, Q.; Wu, H.; Khan, U.; Han, X. Programmable Spin Logic Based on Spin Hall Effect in a Single Device. *Adv. Electron. Mater.* **2017**, *3* (3), 1600282.

(5) Wang, X.; Wan, C.; Kong, W.; Zhang, X.; Xing, Y.; Fang, C.; Tao, B.; Yang, W.; Huang, L.; Wu, H.; et al. Field-Free Programmable Spin Logics via Chirality-Reversible Spin-Orbit Torque Switching. *Adv. Mater.* **2018**, *30* (31), 1801318.

(6) Liu, L.; Pai, C.-F.; Ralph, D. C.; Buhrman, R. A. Magnetic Oscillations Driven by the Spin Hall Effect in 3-Terminal Magnetic Tunnel Junction Devices. *Phys. Rev. Lett.* **2012**, *109* (18), 186602.

(7) Zhu, L.; Ralph, D. C.; Buhrman, R. A. Highly Efficient Spin-Current Generation by the Spin Hall Effect in $Au_{1-x}Pt_x$. *Phys. Rev. Appl.* **2018**, *10* (3), No. 031001.

(8) Sinova, J.; Valenzuela, S. O.; Wunderlich, J.; Back, C. H.; Jungwirth, T. Spin Hall effects. *Rev. Mod. Phys.* **2015**, *87* (4), 1213.

(9) Hoffmann, A. Spin Hall Effects in Metals. *Ieee Transactions on Magnetics* **2013**, *49* (10), 5172−5193.

(10) Liu, L.; Pai, C.-F.; Li, Y.; Tseng, H. W.; Ralph, D. C.; Buhrman, R. A. Spin-Torque Switching with the Giant Spin Hall Effect of Tantalum. *Science* **2012**, *336* (6081), 555−558.

(11) Gomez, J. E.; Zerai Tedlla, B.; Alvarez, N. R.; Alejandro, G.; Goovaerts, E.; Butera, A. Spin transport parameters in $Ni_{80}Fe_{20}$/Ru and $Ni_{80}Fe_{20}$/Ta bilayers. *Phys. Rev. B* **2014**, *90* (18), 184401.

(12) Ando, K.; Takahashi, S.; Harii, K.; Sasage, K.; Ieda, J.; Maekawa, S.; Saitoh, E. Electric manipulation of spin relaxation using the spin Hall effect. *Phys. Rev. Lett.* **2008**, *101* (3), 036601.

(13) Liu, L.; Moriyama, T.; Ralph, D. C.; Buhrman, R. A. Spin-Torque Ferromagnetic Resonance Induced by the Spin Hall Effect. *Phys. Rev. Lett.* **2011**, *106* (3), 036601.

(14) Guo, G. Y.; Murakami, S.; Chen, T. W.; Nagaosa, N. Intrinsic spin Hall effect in platinum: First-principles calculations. *Phys. Rev. Lett.* **2008**, *100* (9), 096401.

(15) Pai, C.-F.; Liu, L.; Li, Y.; Tseng, H. W.; Ralph, D. C.; Buhrman, R. A. Spin transfer torque devices utilizing the giant spin Hall effect of tungsten. *Appl. Phys. Lett.* **2012**, *101* (12), 122404.

(16) Wu, H.; Zhang, P.; Deng, P.; Lan, Q.; Pan, Q.; Razavi, S. A.; Che, X.; Huang, L.; Dai, B.; Wong, K.; et al. Room-Temperature Spin-Orbit Torque from Topological Surface States. *Phys. Rev. Lett.* **2019**, *123* (20), 207205.

(17) Han, J.; Richardella, A.; Siddiqui, S. A.; Finley, J.; Samarth, N.; Liu, L. Room-Temperature Spin-Orbit Torque Switching Induced by a Topological Insulator. *Phys. Rev. Lett.* **2017**, *119* (7), 077702.

(18) Mellnik, A. R.; Lee, J. S.; Richardella, A.; Grab, J. L.; Mintun, P. J.; Fischer, M. H.; Vaezi, A.; Manchon, A.; Kim, E. A.; Samarth, N.; et al. Spin-transfer torque generated by a topological insulator. *Nature* **2014**, *511* (7510), 449.

(19) Gradhand, M.; Fedorov, D. V.; Zahn, P.; Mertig, I. Spin Hall angle versus spin diffusion length: Tailored by impurities. *Phys. Rev. B* **2010**, *81* (24), 245109.

(20) Niimi, Y.; Morota, M.; Wei, D. H.; Deranlot, C.; Basletic, M.; Hamzic, A.; Fert, A.; Otani, Y. Extrinsic Spin Hall Effect Induced by Iridium Impurities in Copper. *Phys. Rev. Lett.* **2011**, *106* (12), 126601.

(21) Qiu, X.; Narayanapillai, K.; Wu, Y.; Deorani, P.; Yang, D.-H.; Noh, W.-S.; Park, J.-H.; Lee, K.-J.; Lee, H.-W.; Yang, H. Spin−orbit-torque engineering via oxygen manipulation. *Nat. Nanotechnol.* **2015**, *10* (4), 333−338.

(22) Zhu, L.; Li, J.; Zhu, L.; Xie, X. Boosting Spin-Orbit-Torque Efficiency in Spin-Current-Generator/Magnet/Oxide Superlattices. *Phys. Rev. Appl.* **2022**, *18* (6), 064052.

(23) Wei, D. H.; Niimi, Y.; Gu, B.; Ziman, T.; Maekawa, S.; Otani, Y. The spin Hall effect as a probe of nonlinear spin fluctuations. *Nat. Commun.* **2012**, *3* (1), 1058.

(24) Ou, Y. X.; Ralph, D. C.; Buhrman, R. A. Strong Enhancement of the Spin Hall Effect by Spin Fluctuations near the Curie Point of Fe_xPt_{1-x} Alloys. *Phys. Rev. Lett.* **2018**, *120* (9), 097203.

(25) Wu, P.-H.; Qu, D.; Tu, Y.-C.; Lin, Y.-Z.; Chien, C. L.; Huang, S.-Y. Exploiting Spin Fluctuations for Enhanced Pure Spin Current. *Phys. Rev. Lett.* **2022**, *128* (22), 227203.

(26) Saglam, H.; Zhang, W.; Jungfleisch, M. B.; Sklenar, J.; Pearson, J. E.; Ketterson, J. B.; Hoffmann, A. Spin transport through the metallic antiferromagnet FeMn. *Phys. Rev. B* **2016**, *94* (14), No. 140412.

(27) Frangou, L.; Oyarzun, S.; Auffret, S.; Vila, L.; Gambarelli, S.; Baltz, V. Enhanced Spin Pumping Efficiency in Antiferromagnetic IrMn Thin Films around the Magnetic Phase Transition. *Phys. Rev. Lett.* **2016**, *116* (7), 077203.

(28) Wang, X.; Wan, C.; Liu, Y.; Shao, Q.; Wu, H.; Guo, C.; Fang, C.; Guang, Y.; Yang, W.; He, C.; et al. Spin transmission in IrMn through measurements of spin Hall magnetoresistance and spin-orbit torque. *Phys. Rev. B* **2020**, *101* (14), 144412.

(29) Du, C. H.; Wang, H. L.; Yang, F. Y.; Hammel, P. C. Systematic variation of spin-orbit coupling with d-orbital filling: Large inverse spin Hall effect in 3d transition metals. *Phys. Rev. B* **2014**, *90* (14), No. 140407.

(30) Qu, D.; Huang, S. Y.; Chien, C. L. Inverse spin Hall effect in Cr: Independence of antiferromagnetic ordering. *Phys. Rev. B* **2015**, *92* (2), No. 020418.

(31) Baltz, V.; Manchon, A.; Tsoi, M.; Moriyama, T.; Ono, T.; Tserkovnyak, Y. Antiferromagnetic spintronics. *Rev. Mod. Phys.* **2018**, *90* (1), 015005.

(32) Sawabu, M.; Ohashi, M.; Ohashi, K.; Miyagawa, M.; Kubota, T.; Takanashi, K. The electrical resistivity of epitaxially deposited chromium films. *J. Phys.: Conf. Ser.* **2017**, *871*, 012002.

(33) Mattson, J.; Brumitt, B.; Brodsky, M. B.; Ketterson, J. B. Magnetotransport studies of epitaxial Cr thin films. *J. Appl. Phys.* **1990**, *67* (9), 4889−4891.

(34) Fang, C.; Wan, C. H.; Yang, B. S.; Qin, J. Y.; Tao, B. S.; Wu, H.; Zhang, X.; Han, X. F.; Hoffmann, A.; Liu, X. M.; et al. Determination of spin relaxation times in heavy metals via second-harmonic spin injection magnetoresistance. *Phys. Rev. B* **2017**, *96* (13), 134421.

(35) Liu, L. Q.; Chen, C. T.; Sun, J. Z. Spin Hall effect tunnelling spectroscopy. *Nat. Phys.* **2014**, *10* (8), 561.

(36) Jedema, F. J.; Filip, A. T.; van Wees, B. J. Electrical spin injection and accumulation at room temperature in an all-metal mesoscopic spin valve. *Nature* **2001**, *410* (6826), 345−348.

(37) Takahashi, S.; Maekawa, S. Spin injection and detection in magnetic nanostructures. *Phys. Rev. B* **2003**, *67* (5), 052409.

(38) Bass, J.; Pratt, W. P. Spin-diffusion lengths in metals and alloys, and spin-flipping at metal/metal interfaces: an experimentalist's critical review. *J. Phys.: Condens. Matter* **2007**, *19* (18), 183201.

(39) Parkin, S. S. P.; Kaiser, C.; Panchula, A.; Rice, P. M.; Hughes, B.; Samant, M.; Yang, S. H. Giant tunnelling magnetoresistance at room temperature with MgO (100) tunnel barriers. *Nat. Mater.* **2004**, *3* (12), 862−867.

(40) Han, X.; Wang, X.; Wan, C.; Yu, G.; Lv, X. Spin-orbit torques: Materials, physics, and devices. *Appl. Phys. Lett.* **2021**, *118* (12), 120502.

(41) Shao, Q. M.; Li, P.; Liu, L. Q.; Yang, H.; Fukami, S.; Razavi, A.; Wu, H.; Wang, K.; Freimuth, F.; Mokrousov, Y.; et al. Roadmap of Spin-Orbit Torques. *IEEE Trans. Magn.* **2021**, *57* (7), 800439.

(42) Kondo, J. Anomalous Hall Effect and Magnetoresistance of Ferromagnetic Metals. *Prog. Theor. Phys.* **1962**, *27* (4), 772−792.

(43) Gu, B.; Ziman, T.; Maekawa, S. Theory of the spin Hall effect, and its inverse, in a ferromagnetic metal near the Curie temperature. *Phys. Rev. B* **2012**, *86* (24), No. 241303.

(44) Okamoto, S.; Egami, T.; Nagaosa, N. Critical Spin Fluctuation Mechanism for the Spin Hall Effect. *Phys. Rev. Lett.* **2019**, *123* (19), 196603.

(45) Wölfle, P.; Ziman, T. Theory of record thermopower near a finite temperature magnetic phase transition in IrMn. *Phys. Rev. B* **2021**, *104* (5), 054441.

(46) Okamoto, S.; Nagaosa, N. Critical enhancement of the spin Hall effect by spin fluctuations. *arXiv* **2023**, DOI: 10.48550/arXiv.2308.09636.

(47) Onoda, S.; Sugimoto, N.; Nagaosa, N. Quantum transport theory of anomalous electric, thermoelectric, and thermal Hall effects in ferromagnets. *Phys. Rev. B* **2008**, *77* (16), 165103.

(48) Miyazaki, T.; Tezuka, N. Giant magnetic tunneling effect in Fe/Al2O3/Fe junction. *J. Magn. Magn. Mater.* **1995**, *139* (3), L231.

(49) Yakata, S.; Ando, Y.; Miyazaki, T.; Mizukami, S. Temperature dependences of spin-diffusion lengths of Cu and Ru layers. *Jpn. J. Appl. Phys., Part 1* **2006**, *45* (5A), 3892.

(50) Isasa, M.; Villamor, E.; Hueso, L. E.; Gradhand, M.; Casanova, F. Temperature dependence of spin diffusion length and spin Hall angle in Au and Pt. *Phys. Rev. B* **2015**, *91* (1), 024402.

(51) Bloch, F. For electric Resistance law at low Temperatures. *Z. Phys.* **1930**, *59* (3−4), 208−214.

(52) Ziman, J. M. *Electrons and Phonons: The Theory of Transport Phenomena in Solids*; Oxford University Press, 2001.

(53) Baber, W. G. The contribution to the electrical resistance of metals from collisions between electrons. *Proc. R. Soc. A* **1937**, *158* (A894), 0383−0396.